


SCIENTIFIC REPORTS



OPEN

Chemical and kinetic insights into the Thermal Decomposition of an Oxide Layer on Si(111) from Millisecond Photoelectron Spectroscopy

J.-J. Gallet^{1,2}, M. G. Silly², M. El Kazzi^{2,4}, F. Bournel^{1,2}, F. Sirotti^{2,3} & F. Rochet^{1,2}

Despite thermal silicon oxide desorption is a basic operation in semiconductor nanotechnology, its detailed chemical analysis has not been yet realized via time-resolved photoemission. Using an advanced acquisition system and synchrotron radiation, heating schedules with velocities as high as 100 K.s^{-1} were implemented and highly resolved Si 2p spectra in the tens of millisecond range were obtained. Starting from a Si(111)- 7×7 surface oxidized in O_2 at room temperature (1.4 monolayer of oxygen), changes in the Si 2p spectral shape enabled a detailed chemical analysis of the oxygen redistribution at the surface and of the nucleation, growth and reconstruction of the clean silicon areas. As desorption is an inhomogeneous surface process, the Avrami formalism was adapted to oxide desorption via an original mathematical analysis. The extracted kinetic parameters (the Avrami exponent equal to ~ 2 , the activation energy of $\sim 4.1 \text{ eV}$ and a characteristic frequency) were found remarkably stable within a wide ($\sim 110 \text{ K}$) desorption temperature window, showing that the Avrami analysis is robust. Both the chemical and kinetic information collected from this experiment can find useful applications when desorption of the oxide layer is a fundamental step in nanofabrication processes on silicon surfaces.

Since the earlier experimental works of D'Evelyn *et al.*¹ and Engstrom *et al.*² the study of the thermal decomposition of silicon oxide layers on silicon has remained an active field of research, both at experimental^{3–17} and theoretical^{18–21} levels. Indeed, volatile SiO (SiO_g) production is a key feature of nanoelectronics processes, naturally relative to silicon surface cleaning^{22,23}, but also to nano-fabrication^{24–28}. Microscopy studies pointed to a spatially inhomogeneous process both on Si(001)^{9–11,14,15,13} and (111) surfaces^{12,16}. Clean voids appear randomly on the oxidized surface, leaving oxide patches whose thickness does not change, while surface pitting is observed in the clean areas. The later observation suggests that silicon atoms from the clean areas are consumed in the reaction and that clean areas grow via reaction of silicon monomers reaching the void periphery where they react with the oxide to form SiO_g .

Consequently, four steps for oxide decomposition are envisaged^{9,10,13,16}:

- creation of a mobile Si monomer (step 1);
- diffusion to the void boundary (step 2);
- reaction of mobile Si with SiO_2 at the void boundary to form SiO_x suboxide species precursor to desorption (step 3);
- desorption of SiO_g (step 4).

¹Sorbonne Universités, UPMC Univ. Paris 06, and CNRS UMR 7614, Laboratoire de Chimie Physique Matière et Rayonnement (LCPMR), F-75005, Paris, France. ²Synchrotron SOLEIL, L'Orme des Merisiers, Saint-Aubin, BP 48, F-91192, Gif-sur-Yvette, France. ³Laboratoire de Physique de la Matière Condensée, CNRS and Ecole Polytechnique, Université Paris Saclay, F- 91128, Palaiseau, France. ⁴Present address: Paul Scherrer Institut, 5232, Villigen-PSI, Switzerland. Correspondence and requests for materials should be addressed to F.R. (email: francois.rochet@upmc.fr)

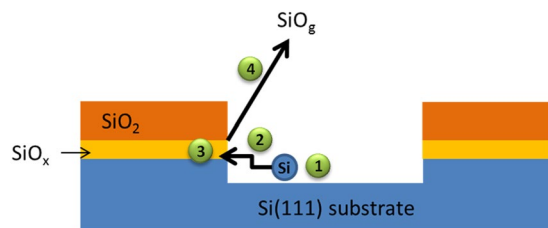


Figure 1. Schematic illustration of the thermal decomposition of oxide layers mediated by silicon monomer formation (step 1), surface mass transport (step 2) and formation of gaseous SiO (SiO_g) (steps 3 and 4) by reaction at the periphery of the clean areas. SiO_x represents the interface suboxide layer (Si^{3+} , Si^{2+} and Si^{1+}) and SiO_2 the fully oxidized silicon atoms (Si^{4+}).

The thermal decomposition of ultra-thin oxidized layers (< 1 ML of oxygen) may be limited by step 1^{9,10}, while thicker thermal oxide layers are apparently limited by steps 3 or 4^{13,16,29}. The void nucleation process itself may depend on the oxide thickness: the density can be constant with time (ultra-thin films⁹), or increase with time for nm-thick thermal films¹³. A pictorial description of the processes occurring during spatially inhomogeneous desorption is given in Fig. 1.

Most thermally programmed desorption (TPD) studies^{1,2,7} were based on the monitoring of the oxygen surface density via the measurement of the volatile SiO_g signal. With the notable exception of ref.⁷, they did not consider explicitly the spatially inhomogeneous nature of the process. In particular, Engstrom *et al.*² interpreted their TPD data in the framework of the Taylor-Weinberg method³⁰, that uses a set of varying velocity heating schedules to extract kinetic data. The Taylor-Weinberg analysis is based on the usual Polanyi-Wigner expression of the reaction rate. At a given coverage, Arrhenius plots provide the value of the activation barrier and of a pseudo-zeroth order pre-factor that are both functions of coverage. One can legitimately wonder whether forcing data from a heterogeneous system into an order-based model (adapted to homogeneous kinetics) is appropriate³¹. Moreover, the analysis made by Engstrom *et al.*² indicates there is significant compensation occurring^{32,33}, which casts some doubts about the validity of the method. In contrast, Kinefuchi *et al.*⁷ took explicitly the inhomogeneous nature of the desorption process into account by considering the Avrami model, which is widely used to analyze the kinetics of phase transition^{34–38}. The Avrami approach considers that the phase transformation (here the de-oxidation process) occurs by nucleation and growth of transformed areas (the clean Si).

TPD experiments that were carried out so far examined the evolution of the oxygen surface density, without going into the details of the chemical bonds appearing or disappearing during the desorption event. In contrast, core-level X-ray photoelectron spectroscopy (XPS) is in principle the ideal technique to study surface kinetics, as it allows an analysis both qualitative (via the binding energy shifts) and quantitative (via the photoemission intensity) of the species present on the surface at a given time, especially when the synchrotron radiation is used, as the high photon flux combined to a fast detection system³⁹ enables the real-time monitoring of reactions with high time resolution. The present Temperature Programmed XPS (TPXPS) study examines in real-time the decomposition of a controlled oxide film formed at room temperature on the Si(111)- 7×7 surface after exposure to O_2 , corresponding to a coverage of 1.4 monolayer (ML). The thermal transformation is monitored via Si 2p photoemission in surface sensitive conditions (see Methods, section “Real-time Photoemission”), because it gives access to the chemical bonding at oxidized silicon interfaces^{40–42}, via the identification of the four oxide states^{40,42}. Moreover information on the clean areas comes from the appearance of the restatom (RA) component⁴³. Therefore spectroscopic information on the clean areas can be provided independently of the SiO_g desorption event.

We adopt a non-isothermal³⁸ approach, with average temperature velocities v_{av} differing by an order of magnitude, between 2.5 K.s^{-1} and 100 K.s^{-1} . Such high temperature velocities are permitted by a short acquisition time of 25 ms per spectrum and a high sampling frequency of 20 Hz (see section S1 in Supplementary Information). A photoemission experiment at this pace is uncommon⁴⁴. It makes the present temperature velocities comparable to those of TPD experiments with quadrupole mass analyzers, for which temperature ramps up to hundreds of K.s^{-1} are not unusual. Such temperature schedules are possible because of the high signal/background ratio for Si 2p core level spectra, and the combination of the fast photoemission detection system synchronized to the temperature measurement, as well as to the electronically controlled annealing process. Similar experiments are currently performed with a time resolution of a few hundreds of milliseconds⁴⁵ using the same detection scheme as ours. Higher speed or better statistics should be achieved with the more complex parallel detection of ref.⁴⁶, capable to handle higher count rates.

For any activated process, a large variation in the ramp velocities, translates to a large temperature window where the transformation (here, surface cleaning) is accomplished. This exploration in temperature enables the identification of chemical reactions that precede, accompany or are responsible for desorption, as their activation energies may differ. This also leads to a more accurate extraction of the kinetic parameters of a properly identified reaction.

After a qualitative chemical analysis of the transformations occurring at the surface (before and after oxide desorption), we perform a kinetic analysis of the desorption event itself based on the Avrami model. The parameter we follow is the fraction of non-transformed matter θ , i.e. the oxide area fraction, using the Si^{4+} (SiO_2) component intensity as a proxy. We give a mathematical treatment of the non-transformed fraction dependence on temperature, including the non-constancy of the temperature ramp velocity. In principle, the kinetic parameters

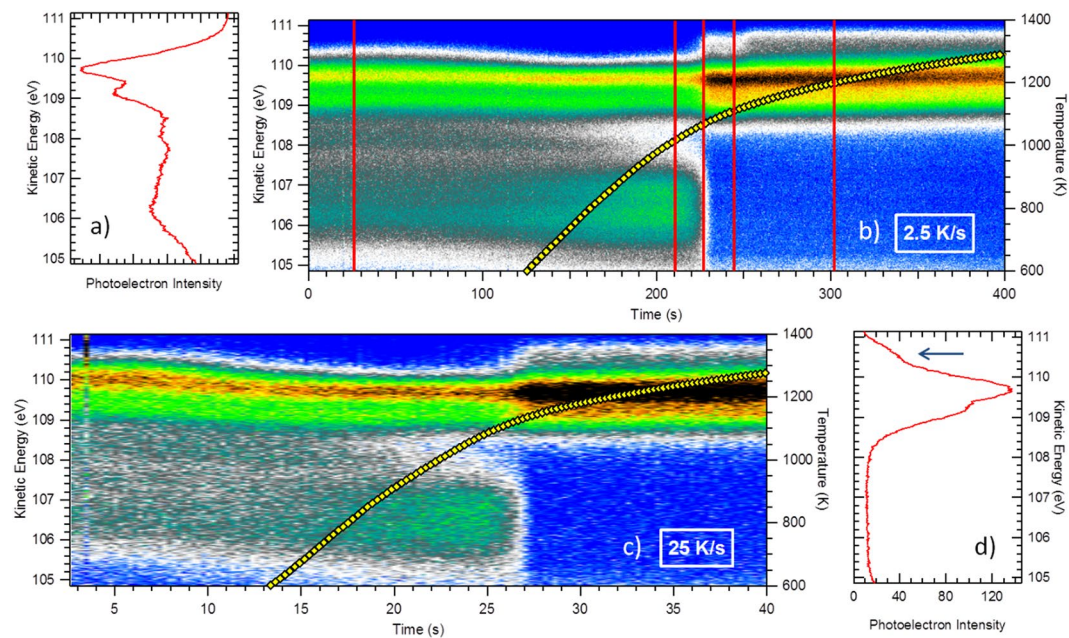


Figure 2. The Si 2p photoemission intensity (raw data, not corrected from the detector response) measured during the thermal annealing process ($v_{av} = 2.5 \text{ K}\cdot\text{s}^{-1}$ in (b), and $v_{av} = 25 \text{ K}\cdot\text{s}^{-1}$ in (c)) is represented in a color scale as function of time (horizontal axes) and of kinetic energy (vertical left axes). Panel (a) corresponds to the initial situation, i.e. the 7×7 surface oxidized at room temperature (1.4 OML). The spectral weight below a kinetic energy of $\sim 108.5 \text{ eV}$ corresponds to the oxidation states. In (d) we show the de-oxidized surface at $\sim 1135 \text{ K}$. The Si 2p core-level is actually a doublet with a spin-orbit splitting of 0.61 eV and a $2p_{3/2}:2p_{1/2}$ branching ratio of 2. The blue arrow indicates the position of the restatom (RA) states of the cleaned surface. The temperature measured during the experiment with a calibrated pyrometer is indicated by the yellow line (right vertical scale). The vertical red solid lines in (b) corresponds to the selected spectra reported in Fig. 3. The photon energy is 210 eV , and the photoelectron emergence angle is 45° with respect to the surface normal. The temperature at time zero is 300 K . The lowest temperature measurable by the pyrometer is 600 K .

can be obtained from one non-isothermal experiment, as in ref.⁷, but the use of various heating schedules helps testing the *robustness* of the Avrami analysis and the *stability* of the kinetic parameters in a wide range of desorption peak temperatures, that encompasses, in particular, the order-disorder 7×7 to “ 1×1 ” phase transition temperature of the clean surface^{47,48}.

Finally, the increasing technological relevance of the Si(111) surface^{49–51} is a further motivation to gain a better chemical understanding and a robust parametrization of the spatially inhomogeneous de-oxidation process, as it can naturally create new opportunities of implementing maskless lithography^{27,28}.

Results

Spectral analysis. In Fig. 2, the 3D maps of the photoemission intensity (raw data, not corrected for detector response, see Methods) versus kinetic energy (left vertical axes) and time (bottom horizontal axes) are represented in a color scale for two temperature schedules with average heating velocities $v_{av} = 2.5 \text{ K}\cdot\text{s}^{-1}$ (b) and $v_{av} = 25 \text{ K}\cdot\text{s}^{-1}$ (c). The temperature evolution (right vertical axes) as a function of time is indicated by the yellow line in each case. The photoemission intensity versus kinetic energy spectra measured at the start (surface oxidized at room temperature) and at the end (de-oxidized surface, measured at 1135 K) of the heating process are presented in the panels (a) and (d), respectively. The latter two correspond to the integration of the 20 first and the 50 last spectra of the 3D maps, respectively.

For the two different v_{av} , the main features are similar: the oxide state components at lower kinetic energies suddenly disappear during the heating process. At the same time the surface component related to the restatoms (RA) of the clean surface, indicated by a blue arrow in Fig. 2(d), appears at higher kinetic energy than the bulk peak.

For the slow heating schedule of $2.5 \text{ K}\cdot\text{s}^{-1}$, four selected Si 2p spectra measured in the “snapshot mode” at significant times indicated by red vertical lines in Fig. 2 are reported in Fig. 3. Each spectrum is integrated over a time period of 250 ms . The detector response is now taken into account, after calculating the ratio between a spectrum measured in the sweep mode and one measured in the snapshot mode. For the sake of comparison, we add two spectra measured in the sweep mode at room temperature, one of the oxygen covered surface and one of the cleaned one. Detailed information on the fitting procedures is given in the SI, section S4. For the oxidized surface, the four oxidation states Si^{n+} , where $n = \{1, 2, 3, 4\}$ is the number of oxygen ligands around the Si atom, are seen, shifted to higher binding energy from the elemental silicon line Si^0 by $\sim +0.9 \text{ eV}$ per O ligand^{40–42,52}. For the oxidized interfaces, the main line Si^0 is accompanied by two satellite lines whose relative binding energy is

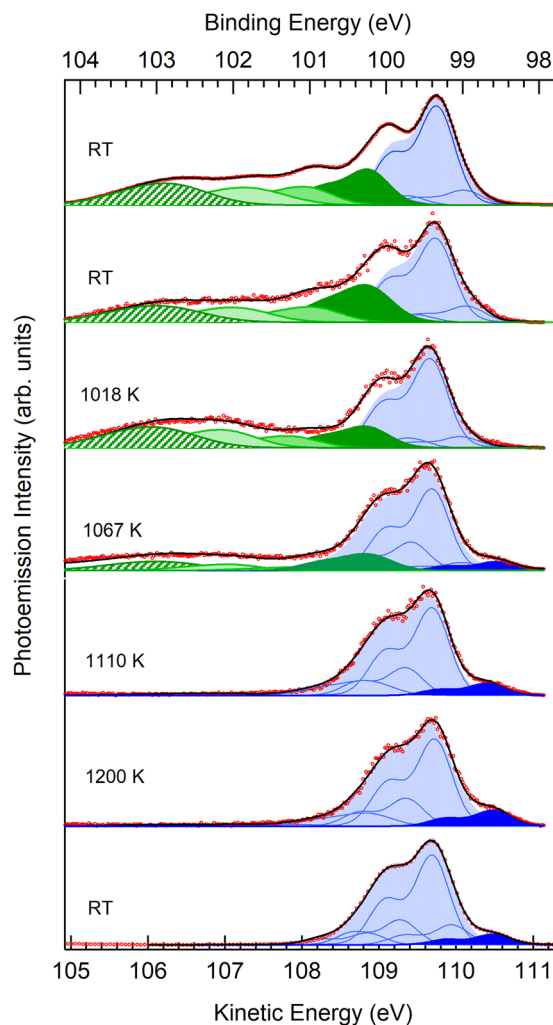


Figure 3. Selected spectra measured during the oxide layer desorption corresponding to the heating schedule ($v_{av} = 2.5 \text{ K.s}^{-1}$). The top and bottom spectra were acquired in sweep mode at room temperature. They correspond to the initial surface (1.4 ML of oxygen deposited at room temperature) exhibiting the contribution of the four oxidation states at higher binding energy (from dark green Si^{1+} to hatched green Si^{4+}) than that of the bulk elemental silicon component (light blue shaded) and to the de-oxidized surface, where the restatom (RA) surface states (at lower binding energy than the bulk line, dark blue shaded) are clearly apparent. Intermediate panels are spectra measured in time resolved mode (the so-called snapshot mode, the spectra are corrected from detector distortions) along with their corresponding spectral reconstruction. At 1067 K the component shifted by -0.9 eV from the main elemental Si component (dark green shaded) is due to two contributions, the Si^{1+} oxidation state, and a clean surface state (see text). Note the increase in RA intensity from 1110 K to 1200 K (7×7 to “ 1×1 ” transition).

shifted by -0.4 and $+0.3 \text{ eV}$ ⁵³. For the cleaned surface, the present instrumental resolution (125 meV) does not make it possible to reveal the Si 2p fine structure reported and discussed in refs^{43,54}. Notwithstanding, we can clearly distinguish the restatom component (RA) shifted to lower binding from the main bulk line Si^0 by $\sim -0.7 \text{ eV}$ ⁴⁰⁻⁴². Other minor components at about -0.3 , $+0.3$ and $+0.9 \text{ eV}$ from Si^0 must be introduced in the fitting procedure. The latter one (maybe a shakeup^{43,55}), overlaps in energy with the Si^{1+} state of the oxidized surface (see Fig. 2, and more especially the 1067 K spectrum where both oxidized and cleaned areas coexist). This leads to a vertical, constant offset in the Si^{1+} intensity after the surface is fully cleaned. Consequently, in Fig. 4, the Si^{1+} intensity is set to zero after the desorption event.

The temperature dependence of the Si^{n+} intensities, along with that of the RA component is reported in Fig. 4 as a function of temperature, for two illustrative heating schedules, the slow one ($v_{av} = 2.5 \text{ K.s}^{-1}$) reported in panel (a) and a four times faster one ($v_{av} = 10 \text{ K.s}^{-1}$) reported in panel (b). Specific temperature curves of the RA and Si^{4+} components for the various v_{av} are reported in Figs 5 and 6, respectively. The “desorption temperature interval” defined by the 95-5% intensity of the Si^{4+} component is given in Table 1.

Concerning the former point, different reaction channels, with different activation energies, can be explored when high velocity ramps are applied, as kinetics dominates thermodynamics. When the 7×7 reconstructed surface is oxidized at room temperature, as is the case here, one obtains a relatively even distribution of

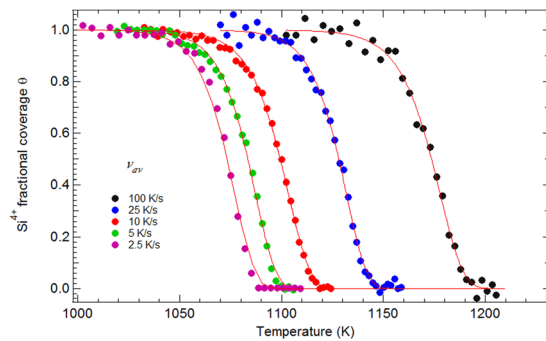


Figure 6. Dependence of the Si^{4+} fractional coverage θ (squares) with temperature for five different heating schedules with average velocities ν_{av} . Red solid lines are fits obtained with the 3-parameter Avrami model. Corresponding parameters are given in Table 1 together with the χ^2 .

ν_{av} ($\text{K}\cdot\text{s}^{-1}$)	desorption interval 95–5% Si^{4+} (K)	T_{peak} (K)	ν_{peak} ($\text{K}\cdot\text{s}^{-1}$)	n	E_{eff} (eV)	k_0 (s^{-1})	χ^2 ($\times 10^{-3}$)
2.5	1049–1084	1073.6	2.6	2.148	4.125	2.42×10^{18}	5.166
5	1057–1098	1087.4	4.7	2.151	4.060	1.44×10^{18}	10.11
10	1071–1115	1103.3	8.8	2.017	4.061	1.43×10^{18}	7.5
25	1102–1143	1131.5	20.6	2.200	4.200	4.69×10^{18}	20.78
100	1144–1190	1177.7	91.6	2.061	4.203	3.75×10^{18}	27.24
Average	—	—	—	2.115	4.13	2.75×10^{18}	—

Table 1. The desorption temperature interval is comprised between 95% and 5% of the Si^{4+} component intensity (Fig. 6). The temperature of maximum desorption rate (T_{peak}) corresponds to a fractional coverage equal to $\frac{1}{e} = 0.368^{38}$. ν_{peak} is the heating velocity at T_{peak} . Avrami exponent (n), coefficient (k_0) and effective activation energy (E_{eff}) are deduced from the fits of Fig. 6. The fitting method is described in “Methods”, subsection “Fitting of the desorption curves with a non-isothermal Avrami Kinetic Model”. The Chi-square value (χ^2) is also given.

affect the surface reconstruction of the cleaned areas (and we shall see it is indeed the case). Therefore, spectroscopic information on the suboxide distribution and on the surface state intensities (in the clean areas) is decisive for understanding the desorption process.

Let us first focus on the behavior of the Si suboxides states with temperature. For the slow heating schedule of $\nu_{av} = 2.5 \text{ K}\cdot\text{s}^{-1}$, see Fig. 4(a), the desorption temperature interval is 1049–1084 K. However, modifications in the oxide state distribution are already seen from $\sim 850 \text{ K}$. While the Si^{4+} state intensity increases slowly, the increase in the Si^{3+} state intensity is much steeper. The Si^{1+} state decreases continuously until the desorption event. In contrast with the other suboxide states Si^{3+} and Si^{1+} , the temperature behavior of the Si^{2+} component is different. It decreases continuously and becomes non-measurable at the onset of oxide desorption (1050 K), that is $\sim 30 \text{ K}$ before the surface is fully cleaned from its oxide (when the Si^{4+} intensity is zero).

For a faster heating schedule of $\nu_{av} = 10 \text{ K}\cdot\text{s}^{-1}$, Fig. 4(b), the desorption temperature interval is shifted to higher temperature (1071–1115 K). As expected for activated processes, kinetic events are function of both time and temperature: the transition shifts to higher temperature when heated at a higher rate, because of the reduced time spent at each temperature. The behaviors of the four Si oxidation states are similar to those observed at a slower ν_{av} of $2.5 \text{ K}\cdot\text{s}^{-1}$. The Si^{2+} signal becomes unmeasurable at 1081 K, that is $\sim 34 \text{ K}$ before the Si^{4+} intensity goes to zero, as observed for the slower heating schedule.

The same type of Si/SiO₂ interface, with dominating Si^{3+} and Si^{1+} suboxide states, is formed for the two different heating schedules, thus the chemistry of the Si/SiO₂ interface seems independent of the thermal history. After O₂ exposure at room temperature, the dimer-adatom-stacking fault (DAS) structure is decorated by O atoms inserted within the silicon-silicon bonds. Upon heating, the oxidized DAS is destroyed, and the characteristic thermal SiO₂/Si(111) interface forms⁴². Si^{1+} and Si^{3+} states are preponderant, simply because of the orientation of the surface (in a diamond cubic lattice, a cut of the (111) plane give surface atoms exhibiting only one or three dangling bonds). Oxygen atoms migrate at the surface, but do not leave it at temperatures lower than the Si^{4+} desorption front, as shown by the O 1s intensity curve versus T plotted in the supporting information, section S3, Figure S3.

If we now concentrate on the RA intensity curve (pink line in Fig. 4) of the slow heating schedule of $2.5 \text{ K}\cdot\text{s}^{-1}$, we observe it starts to increase at $\sim 1000 \text{ K}$ (Fig. 4(a)), that is $\sim 50 \text{ K}$ before the desorption interval, as defined before (5–95% of Si^{4+} intensity). This means that the suboxide rearrangement leaves clean silicon patches that make possible the appearance of the tri-coordinated adatoms (AD) and of RA, and charge transfer from the AD (in excess with respect to RA) to the RA dangling bonds, that become fully occupied⁵⁷. This is a clear proof of the formation of de-oxidized areas before the SiO₂ desorption event. These areas are likely the nuclei from which the

desorption process (depicted in Fig. 1) will start. In this regime, the nuclei are already formed before the transformation. Once oxygen atoms start to migrate away, a corner hole opens due to AD movements, as depicted in the work of Ohdomari and coworkers⁵⁸, leading to the DAS reconstruction. With the present slow heating schedule, the 7×7 DAS structure has enough time to form. Naturally the RA intensity shows a steep increase at the desorption edge, where the oxide state intensities suddenly fall. When we consider now the faster (10 K.s^{-1}) schedule (Fig. 4(b)), we observe that the RA signal starts to take off within the desorption interval. Due to the high temperature rate the system may have not enough time to produce well-ordered 7×7 DAS areas before the desorption event.

After the desorption event, the behavior of the RA intensity as a function of temperature is illustrated in Fig. 5 for three different heating. Very interestingly, a second rise in intensity of the RA is seen at about 1128 K (midpoint) for the slower ramp with $v_{av} = 2.5 \text{ K.s}^{-1}$. This point was also clearly visible in the 3D map of Fig. 2(b) and in the spectra shown in Fig. 3 (compare the 1110 K and 1200 K spectra). The temperature of 1130 K is precisely that of the 7×7 DAS \rightarrow “ 1×1 ” phase transition^{47,48}, above which an increase in the RA intensity was observed by Paggel *et al.* in the Si 2p spectrum⁵⁹. These authors proposed that the so-called “ 1×1 ” is in fact a disordered 2×2 reconstruction on top of an ideal 1×1 bilayer of the bulk-terminated Si(111) surface, presenting one RA and one AD per unit cell. The electron in the AD dangling bond can be transferred to the RA one that becomes doubly occupied, and thus negatively charged, which also leads to a surface core-level state at lower binding energy than that of the bulk component. The RA coverage of the 2×2 reconstruction is $\frac{1}{4}$ ML (0.25 ML), higher than that of the 7×7 DAS that amounts to $\frac{7}{49}$ ML (0.14 ML), and therefore the increase in the surface state intensity can be understood. Note that the non-linear optical spectroscopy study by Höfer *et al.*⁶⁰ indicates a substantial increase in the dangling bond surface density above the transition temperature.

The remarkable point is the fact that the 7×7 DAS to “ 1×1 ” transition temperature changes with the ramp velocity (Fig. 5). For the 5 K.s^{-1} schedule, the RA intensity jump at the 7×7 DAS to “ 1×1 ” transition is still visible, but at a distinctly smaller value of $\sim 1120 \text{ K}$ (midpoint). For an activated kinetic process, involving dimer breaking and elimination of the DAS, the opposite would be expected. Our result suggests that the clean areas of the $v_{av} = 10 \text{ K.s}^{-1}$ ramp are composed of less ordered 7×7 DAS surface cells that transit to “ 1×1 ” below their expected thermodynamic phase transition temperature of $\sim 1130 \text{ K}$. The formation of strained, smaller DAS cells^{61–63} can be equally envisaged. Note that the RA signal takes off at 1050 K, which corresponds to the onset of the Si^{4+} decay, see Fig. 6, which contrasts with the 2.5 K.s^{-1} ramp for which the nucleation of clean areas with significant RA intensity predated the desorption process.

For the $v_{av} \geq 10 \text{ K.s}^{-1}$ ramps, the RA intensity curves do not present the characteristic jump of the 7×7 to “ 1×1 ” phase transition. The RA intensity of the 10 K.s^{-1} ramp saturates at 1120 K (when the Si^{4+} intensity is zero). For the faster schedules the surface becomes clean at temperatures of 1150 K (25 K.s^{-1}) and 1190 K (100 K.s^{-1}), that are significantly above the 7×7 to “ 1×1 ” transition temperature. As the 7×7 DAS to “ 1×1 ” transition temperature decreases below the “thermodynamic” one when the temperature rate increases, there is no reason to believe that the 7×7 is formed in this case.

This spectroscopic information gives clues on the nucleation of the clean areas and on their reconstruction. The faster the ramp the more disordered (or strained) the de-oxidized patches, and the 7×7 DAS is no more an intermediate. The question that arises here is whether this has an impact on the kinetic parameters of oxide desorption, as the Avrami exponent and effective activation energy depend on the nucleation process.

Kinetic analysis. Time-resolved Si 2p spectroscopy gives clear evidence that oxygen rearrangement and elimination of the DAS structure leads to a characteristic SiO_x interface prior to de-oxidation. During the desorption process the spectroscopic data indicate that the Si^{4+} , Si^{3+} and Si^{1+} oxide disappear at the same pace. Naturally this can be accounted for by the growth of clean silicon voids at the expense of the ultra-thin thermal oxide (Fig. 1). Consequently, the most intense Si^{4+} component is used as a “proxy” to extract the kinetic parameters of the oxide desorption process.

In Fig. 6 we plot the Si^{4+} fractional coverage as a function of temperature for the five different temperature schedules (see Methods, subsection “Real-time Photoemission”). The temperature of the maximum desorption rate (T_{peak}) reached at a fractional coverage θ of $\sim 1/e$ (0.37)³⁸ is reported in Table 1 as well as the corresponding temperature velocity v_{peak} (calculated using eq. 8 in the SI). The desorption fronts (midpoints) shift to higher values for increasing heating velocities by about 110 K (from ~ 1070 to $\sim 1180 \text{ K}$). This vast temperature extension warrants a good evaluation of the robustness of the Avrami modelling and the stability of the kinetic parameters over the 7×7 to “ 1×1 ” thermodynamic transition temperature of $\sim 1128 \text{ K}$ as discussed before. The desorption fronts are fitted by the mathematical formulae given in “Methods”, subsection “Fitting of the desorption curves with a non-isothermal Avrami kinetic model” (Eqs (5) and (6)), that are an adaptation of the Avrami formalism to the present non-isothermal case where the heating schedules are not linear with time. The fitting parameters are the Avrami exponent n , on the one hand, and the effective activation energy E_{eff} and the pre-exponential factor k_0 (a frequency) of the Avrami coefficient k , on the other hand (see “Methods”, subsection “Fitting of the desorption curves with a non-isothermal Avrami kinetic model”). All three parameters were let free. We observed that the value of n shapes the desorption fronts. For instance, by forcing n to 1 (see SI, section S5, Figure S5), we could not fit properly the steepness of the desorption front. Indeed, a first-order reaction accounts for a homogeneous system, which is definitely not the case here³¹. The fitting values are collected in Table 1.

Table 1 shows that n close to 2 (the average is 2.1) gives excellent fits of the desorption steps for all the heating schedules (the increase in χ^2 observed for the faster temperature programs is due to the “noisy” Si^{4+} intensities and not to the fitting accuracy), showing that the Avrami modelling is robust through a wide T_{peak} range. For a 2D system, an n value of 2 is indicative of “simultaneous nucleation” (see “Methods”, subsection “Fitting of the desorption curves with a non-isothermal Avrami kinetic model”) i.e. desorption nuclei (i.e. clean surface area)

preexist (as shown by the RA intensity versus T curve of the 2.5 K.s^{-1} ramp in Fig. 4), or form immediately on the surface when oxygen desorbs. In such a case k_0 is proportional to \sqrt{N} where N is the density of nuclei, and the activation energy E_{eff} is simply E_G , that of the void growth velocity v_G . We find that E_{eff} ($=E_G$) is $4.1 \pm 0.1 \text{ eV}$. The Avrami model that takes explicitly into account the spatial non-homogeneity of the desorption process, gives a single-valued activation energies, in contrast with the coverage-dependent activation energies of a Taylor-Weinberg analysis². This value is good accord with void growth rate activation energies obtained via microscopy measurements^{13,17} for oxidized Si(001), that are all close to $\sim 4.0 \text{ eV}$, in a vast range of oxide film thicknesses, between ~ 1 and 120 nm . Experimental and theoretical data concern only step 4, in the limit case of “zero coverage”. The experimental activation barrier for SiO_g desorption on Si(111) has an upper bound value of $4.4 \pm 0.15 \text{ eV}$ (Memmert *et al.*³) and a lower bound one of 3.3 eV (Engstrom *et al.*²), the latter one being close to what is found for Si(001)^{1,2,5,6}. Desorption energies were not calculated for the Si(111) surface. The calculated desorption barrier of a single oxygen atom “embedded” in the otherwise clean silicon (001) surface (no oxygen clustering is considered), is in the $3.5\text{--}3.9 \text{ eV}$ range ($3.53\text{--}3.87 \text{ eV}$ in a quantum mechanical calculation^{19,21} and $3.60\text{--}3.80 \text{ eV}$ in a plane wave density functional theory calculation¹⁸).

The stability of the kinetic parameters k_0 and E_{eff} is remarkable and is a valuable clue to understanding the nucleation process. This means that N is about the same for the slow heating schedules and for the faster ones, despite the differences in RA peak appearance. E_{eff} ($=E_G$) is also insensitive to the desorption front (T_{peak}) occurring below or above the 7×7 to “ 1×1 ” phase transition at 1130 K . The nature of the surface reconstruction is unimportant, suggesting that step 1 (adatom formation) and step 2 (adatom diffusion) are not limiting steps. Only step 3 (formation of precursor) or step 4 (SiO_g desorption) matter.

Finally, our fitting procedure leading to the extraction of the three kinetic parameters differs from the Avrami analysis by Kinefuchi and coworkers⁷ who chose deliberately an activation energy equal to that of SiO_g desorption at nearly zero oxygen coverage⁶. This *a priori* choice may lead to a non-integer n exponent between 2 (instantaneous nucleation) and 3 (constant nucleation rate), of unphysical meaning (see “Methods” subsection “Fitting of the desorption curves with a non-isothermal Avrami kinetic model”), unless one concedes it reflects a nucleation rate that decays exponentially with time⁶⁴. Moreover the latter authors used a single heating program (that is sufficient in principle), but did not explore the range of application of their modelling by varying the heating velocities and thus the desorption peak temperatures.

Concluding remarks

We have used thermally programmed XPS (TPXPS) to monitor the de-oxidation process of the 7×7 DAS Si(111) oxidized at room temperature. The combination of the synchrotron radiation high flux and a fast acquisition system synchronized to the temperature measurement and to a controlled heating program, lead to the recording of “chemically meaningful” spectra with a time resolution of 50 ms . The maximum heating velocities we have reached are now competitive with TPD experiments based on mass analysis, and are also comparable to the temperature rise of rapid thermal annealing processes, commonly used in semiconductor surface processing, which warrants a wide range of applications for TPXPS. With respect to previous thermally programmed desorption (TPD) experiments that monitor the SiO_g desorption rates, fast (*ms*) Si 2p spectroscopy gives access to changes in the distribution of the oxidation states, before and during the SiO_g desorption event, to which TPD is obviously blind. TPXPS adds also chemical evidence to the desorption models that microscopies have provided, emphasizing the complementarity of the two approaches.

TPXPS sheds new light on the formation of clean areas by monitoring the intensity of the restatom component. We see that the temperature of the phase transition 7×7 DAS to disordered “ 1×1 ” reconstruction decreases when the temperature velocity increases. Defective 7×7 DAS cells (or maybe smaller DAS cells) might be formed, with a lower transition temperature to the “ 1×1 ”.

Avrami’s nucleation-growth model is implemented through the derivation of mathematical expressions that account for the non-linearity of the heating schedules. This enables us to extract the kinetic parameters (a triplet) that describe the de-oxidation process. The Avrami exponent is close to 2, pointing to a 2D process for which the nucleation of clean areas is instantaneous. The clean area growth activation energy is of $\sim 4.1 \text{ eV}$. The question remains as to whether the limiting step is the desorption of SiO_g into the gas phase, or the formation of a species precursor to desorption by reaction of Si with SiO_2 . Hopefully, this work will stimulate experimental and theoretical studies on the reaction of silicon monomers with the surface of silica. The wide range of heating velocities translates into a $\sim 110 \text{ K}$ temperature window for the desorption fronts (encompassing the static 7×7 DAS to disordered 1×1 transition temperature), within which the fitting parameters are found very stable. The present analysis can find useful applications when desorption of the oxide layer is a fundamental step in nanofabrication processes on silicon surfaces.

Methods

Real-time photoemission. Real-time desorption experiments were performed in the UHV photoemission experimental station of the TEMPO beamline at the SOLEIL synchrotron radiation facility⁶⁵. For the Si 2p spectra (of binding energy $\sim 100 \text{ eV}$) the choice of the photon energy is conditioned by the pass energy (PE) that defines the “snapshot” energy window width (6% of the PE). A width of 6 eV is necessary to encompass the oxidation states, and the elemental silicon components. Therefore, a PE of 100 V was used. As the Scienta SES200 works correctly with photoelectrons of kinetic energies greater than PE, we used a photon energy $h\nu$ of 210 eV to record the Si 2p snapshot window. The inelastic mean free path λ of photoelectrons of kinetic energy $\sim 110 \text{ eV}$ in Si is 5 \AA ⁴⁰. As the takeoff angle of the photoelectrons was 45° from normal, the effective escape depth, $\lambda \times \cos(45^\circ)$, is 3.5 \AA . This value is comparable to the minimum λ , 3.3 \AA , ref.⁴⁰ obtained when the kinetic energy is $\sim 30 \text{ eV}$, i.e. when $h\nu = 130 \text{ eV}$. The overall instrumental resolution was $\sim 125 \text{ meV}$. The Si 2p core-level is actually a doublet

τ_{ramp} (s)	v_{av} (K.s ⁻¹)	T_m (K)	φ (K.s ⁻¹)
400	2.5	1295.4	15.3
200	5	1293.9	29.68
100	10	1278.2	64.64
40	25	1293	164.86
10	100	1324.9	825.28

Table 2. Parameters (T_m and φ) of the heating schedules of duration τ_{ramp} and average velocity v_{av} .

with a spin-orbit splitting of 0.61 eV and a $2p_{3/2}:2p_{1/2}$ branching ratio of 2. For their part, O 1s spectra were measured at a photon energy of 640 eV (see supporting information, section S2).

The (111)-oriented silicon substrates (of dimensions 5 mm × 10 mm × 0.25 mm) were phosphorus-doped (resistivity 10^{-3} Ω.cm), thoroughly degassed overnight at 600 °C and cleaned from their native oxide by Joule heating before exposure to dry oxygen in controlled conditions. To obtain spatially homogeneous and reproducible starting oxygen coverage, the formation of thermal oxide by Joule heating in the presence of O₂ was not considered as practicable because of temperature gradient across the sample and difficulties in keeping the temperature fixed with time. Therefore, the surface oxidation was carried out at room temperature under a pressure of $\sim 5 \times 10^{-8}$ mbar. As in the very initial regime faulted half-cells are the more reactive than unfaulted ones, a homogeneous coverage on both half-cells is obtained at room temperature for O₂ doses of ~ 45 L (1 L = 10^{-6} Torr × s), see ref.⁶⁶ and its supporting information. At such high doses, the oxygen uptake is also very slow, as shown by the adsorption kinetic curve given in Figure S2(a) of the SI. An estimated O coverage of 1.4 ML (1 ML = 7.68×10^{14} atoms/cm²) was obtained. The O 1s spectrum at 45 L (Figure S2(b) of the SI) shows clearly the absence of molecular metastable oxygen^{67,68}, observed at much lower exposure (~ 1 L).

To extract significant kinetic parameters relative to the thermal de-oxidation process, several heating schedules with average ramp velocities v_{av} between ~ 2.5 K/s and ~ 100 K/s were applied to the oxygen covered wafer. Therefore, it was crucial to start with identical surface conditions. In particular, the sample surface must not roughen after repeated oxidation/de-oxidation cycles. This was ensured by (111) oriented wafers: this orientation is stable with respect to step formation during oxide sublimation⁶⁹, in contrast to the (001) orientation that can be heavily etched¹. The room temperature oxidized Si wafers were heated by direct current injection in front of the electron analyzer while performing photoemission experiments. Reproducible and scalable heating rates were performed using predefined voltage shapes from a Tektronix programmable function generator driving a KEPCO power supply [200 W BOP-E] operated as voltage to current amplifier. The temperature was measured for each experiment using a fast response pyrometer “IMPAC IS-12 Si” dedicated to silicon surface measurements (emissivity = 0.67). The “IMPAC IS-12 Si” can only measure temperatures from 600 K.

As Joule heating induces a potential drop dependent on the sample resistance, and hence a shift in the measured kinetic energy of the core level spectrum, we submitted the silicon sample to a “comb-like” voltage ramp, with current pulses of 25 ms and zero bias intervals of 25 ms. High resolution photoemission spectra are obtained at zero bias: the sample is grounded and the Fermi level is the same as that of the analyzer.

The voltage comb was synchronized with the photoemission data acquisition to separate signals obtained during current flow and zero applied voltage. We used the fast acquisition system of the TEMPO beamline³⁹ set at 25 ms/spectrum, corresponding to a snapshot periodicity of 50 ms (measurement at zero bias).

The resulting temperature ramps $T(t)$ were non-linear in the regions of interest (e.g. the desorption event), see the yellow curves in Fig. 2. We fitted the useful part of temperature curve with a function of the type:

$$T(t) = T_m \left(1 - \exp\left(-\frac{\varphi}{T_m} t\right) \right) \quad (1)$$

where $T < T_m$.

The parameters φ and T_m are given in Table 2. Temperature ramps of duration τ_{ramp} are denominated according to their average velocity v_{av} .

The non-constant temperature rates preclude any precise application of classic “Arrhenian” methods such as Kissinger plots^{38,70}. For non-isothermal transformations, Kissinger plots present also the disadvantage of providing only the activation energy, as the determination of the Avrami exponent is cumbersome, and finally inaccurate³⁸.

Fitting of the desorption curves with a non-isothermal Avrami kinetic model. In the Avrami formalism, nuclei are distributed at random and the nucleation and growth laws are given *a priori*. In the isothermal case, the fraction of the untransformed phase θ is given by the simple formula^{34–38}:

$$\theta = e^{-\alpha_{\text{ex}}} \quad (2)$$

where α_{ex} is the so-called extended transformed phase fraction, that is the fractional surface the transformed phase would acquire if the overlap among the growing nuclei were disregarded. For simultaneous or continuous nucleation and provided the growth law is a time power, α_{ex} is expressed as a function of the transformation path $\beta = kt$ function of under the form:

$$\alpha_{ex} = \beta^n = (kt)^n \quad (3)$$

where t , k and n are the running time, the Avrami coefficient (a frequency) and the Avrami exponent (an integer), respectively.

Considering the 2D case, the limiting step is the reaction occurring at the periphery of the clean (circular) areas, and hence the rate is proportional to the radius. By assuming a *constant* growth rate for the transformed phase (v_G is the void radius growth velocity) and simultaneous nucleation (N , the surface density of nuclei is constant), then $\alpha_{ex} = N\pi(v_G t)^2$. In such a case, the Avrami exponent n is equal to 2 and the Avrami coefficient k is simply

$$k = \sqrt{\pi N} v_G \quad (4)$$

When v_G remains constant, but the density of nuclei increases linearly with t , it can be easily shown that the Avrami exponent n is equal to 3 (see section S5 of the SI).

In the case of non-isothermal experiment, we calculate a transformation path (T) (depending on the temperature T) that substitutes that of the isothermal transformation. We assume that the Avrami coefficient k follows an Arrhenian dependence of the type $k = k_0 \exp(-E_{eff}/k_B T)$. Then one obtains (see SI section S5 for the detailed calculation):

$$\beta(T) = \frac{k_0 T_m}{\varphi} \left[-\exp\left(-\frac{E_{eff}}{k_B T_m}\right) \text{Ei}\left(-\frac{E_{eff}}{k_B} \left(\frac{1}{T} - \frac{1}{T_m}\right)\right) + \text{Ei}\left(-\frac{E_{eff}}{k_B T}\right) \right] \quad (5)$$

where T_m (K) and φ (K.s⁻¹) are the fitting parameters of the non-linear temperature schedules reported in Table 2. Ei is the exponential integral $\text{Ei}(x) = -\int_{-x}^{\infty} \frac{e^{-t}}{t} dt$.

The fraction of untransformed matter (T) is simply written as:

$$\theta(T) = \exp(-[\beta(T)]^n) \quad (6)$$

In the fitting procedure of the transformation steps φ and T_m are fixed parameters. The kinetic parameters n (the Avrami exponent), k_0 the pre-exponential factor of the Avrami coefficient and E_{eff} the effective activation energy are let free. With a growth velocity $v_G = v_{G,0} \exp(-\frac{E_G}{k_B T})$, where $v_{G,0}$ is the growth velocity pre-exponential factor, and for instantaneous nucleation, $n = 2$, $k_0 = \sqrt{\pi N} v_{G,0}$ and $E_{eff} = E_G$.

Data Availability. The datasets generated during and/or analyzed during the current study are available from the corresponding author on reasonable request.

References

- D'Evelyn, M. P., Nelson, M. M. & Engel, T. Kinetics of the adsorption of O₂ and of the desorption of SiO on Si(100): A molecular beam, XPS, and ISS study. *Surf. Sci.* **186**, 75–114 (1987).
- Engstrom, J. R., Bonser, D. J., Nelson, M. M. & Engel, T. The reaction of atomic oxygen with Si(100) and Si(111). *Surf. Sci.* **256**, 317–343 (1991).
- Memmert, U. & Ming, L. Y. Comparison between Si(100) and Si(111) in the reaction with oxygen at high temperatures. *Surf. Sci.* **245**, L185–L189 (1991).
- Raschke, M., Bratu, P. & Höfer, U. Optical second-harmonic investigations of the isothermal desorption of SiO from the Si(100) and Si(111) surfaces. *Surf. Sci.* **410**, 351–361 (1998).
- Kinefuchi, I., Yamaguchi, H., Sakiyama, Y. & Matsumoto, Y. Molecular Beam Study on Oxidation of Si(100) Surface with Ozone. in *Rarefied Gas Dynamics: 25th International Symposium on Rarefied Gas Dynamics* (ed. Ivanov, M. S. Rebrov, A. K. Siberian Branch of the Russian Academy of Sciences, N.) 1325–1330 (2007).
- Kinefuchi, I., Yamaguchi, H., Sakiyama, Y., Takagi, S. & Matsumoto, Y. Thermal Decomposition Process of Ultrathin Oxide Layers on Si(100). *Hyomen Kagaku* **29**, 537–542 (2008).
- Kinefuchi, I., Yamaguchi, H., Sakiyama, Y., Takagi, S. & Matsumoto, Y. Inhomogeneous decomposition of ultrathin oxide films on Si(100): application of Avrami kinetics to thermal desorption spectra. *J. Chem. Phys.* **128**, 164712 (2008).
- Tromp, R., Rubloff, G., Balk, P., LeGoues, F. & van Loenen, E. J. High-temperature SiO₂ decomposition at the SiO₂/Si interface. *Phys. Rev. Lett.* **55**, 2332–2335 (1985).
- Johnson, K. & Engel, T. Direct measurement of reaction kinetics for the decomposition of ultrathin oxide on Si(001) using scanning tunneling microscopy. *Phys. Rev. Lett.* **69**, 339–342 (1992).
- Johnson, K. E., Wu, P. K., Sander, M. & Engel, T. The mesoscopic and microscopic structural consequences from decomposition and desorption of ultrathin oxide layers on Si(100) studied by scanning tunneling microscopy. *Surf. Sci.* **290**, 213–231 (1993).
- Wei, Y., Wallace, R. M. & Seabaugh, A. C. Void formation on ultrathin thermal silicon oxide films on the Si(100) surface. *Appl. Phys. Lett.* **69**, 1270 (1996).
- Watanabe, H., Fujita, K. & Ichikawa, M. Thermal decomposition of ultrathin oxide layers on Si(111) surfaces mediated by surface Si transport. *Appl. Phys. Lett.* **70**, 1095 (1997).
- Hibino, H., Uematsu, M. & Watanabe, Y. Void growth during thermal decomposition of silicon oxide layers studied by low-energy electron microscopy. *J. Appl. Phys.* **100**, 113519 (2006).
- Enta, Y., Ogawa, K. & Nagai, T. Void and Nanostructure Formations during Thermal Decomposition of 20-nm-Thick Silicon Oxide Layer on Si(100). *Jpn. J. Appl. Phys.* **52**, 31303 (2013).
- Enta, Y., Nagai, T., Yoshida, T., Ujiie, N. & Nakazawa, H. Decomposition kinetics of silicon oxide layers on silicon substrates during annealing in vacuum. *J. Appl. Phys.* **114**, 114104 (2013).
- Xue, K., Xu, J. B. & Ho, H. P. Nanoscale *in situ* investigation of ultrathin silicon oxide thermal decomposition by high temperature scanning tunneling microscopy. *Nanotechnology* **18**, 485709 (2007).
- Enta, Y., Osanai, S. & Ogasawara, T. Activation energy of thermal desorption of silicon oxide layers on silicon substrates. *Surf. Sci.* **656**, 96–100 (2017).

18. Uchiyama, T., Uda, T. & Terakura, K. Desorption of SiO molecule from the Si(100) surface. *Surf. Sci.* **474**, 21–27 (2001).
19. Choi, C. H., Liu, D.-J., Evans, J. W. & Gordon, M. S. Passive and Active Oxidation of Si(100) by Atomic Oxygen: A Theoretical Study of Possible Reaction Mechanisms. *J. Am. Chem. Soc.* **124**, 8730–8740 (2002).
20. Hemeryck, A., Richard, N., Estève, A. & Djafari Rouhani, M. Active oxidation: Silicon etching and oxide decomposition basic mechanisms using density functional theory. *Surf. Sci.* **601**, 2082–2088 (2007).
21. Arora, P. *et al.* Diffusion of Atomic Oxygen on the Si(100) Surface. *J. Phys. Chem. C* **114**, 12649–12658 (2010).
22. Ishizaka, A. Low Temperature Surface Cleaning of Silicon and Its Application to Silicon MBE. *J. Electrochem. Soc.* **133**, 666 (1986).
23. Takahashi, H. *et al.* Annealing-time dependence in interfacial reaction between poly-Si electrode and HfO₂/Si gate stack studied by synchrotron radiation photoemission and x-ray absorption spectroscopy. *Appl. Phys. Lett.* **89**, 12102 (2006).
24. Enta, Y., Osanai, S. & Yoshida, T. Ring structures formed inside voids in SiO₂ layer on Si(100) during thermal decomposition. *Jpn. J. Appl. Phys.* **55**, 28004 (2016).
25. Cui, Y. & Lieber, C. M. Functional nanoscale electronic devices assembled using silicon nanowire building blocks. *Science* **291**, 851–3 (2001).
26. Yang, Y., Shalav, A., Kim, T. & Elliman, R. G. The effect of annealing temperature, residual O₂ partial pressure, and ambient flow rate on the growth of SiO_x nanowires. *Appl. Phys. A* **107**, 885–890 (2012).
27. Johnson, S., Markwitz, A., Rudolphi, M. & Baumann, H. Nanostructuring of silicon (100) using electron beam rapid thermal annealing. *J. Appl. Phys.* **96**, 605–609 (2004).
28. Fang, F. & Markwitz, A. Controlled fabrication of Si nanostructures by high vacuum electron beam annealing. *Phys. E Low-dimensional Syst. Nanostructures* **41**, 1853–1858 (2009).
29. Irajizad, A., Taghavinia, N., Ahadian, M. & Mashaei, A. Thermal desorption of ultrathin silicon oxide layers on Si(111). *Semicond. Sci. Technol.* **15**, 160–163 (2000).
30. Taylor, J. L. & Weinberg, W. H. A method for assessing the coverage dependence of kinetic parameters: Application to carbon monoxide desorption from iridium (110). *Surf. Sci.* **78**, 259–273 (1978).
31. Khawam, A. & Flanagan, D. R. Solid-state kinetic models: basics and mathematical fundamentals. *J. Phys. Chem. B* **110**, 17315–28 (2006).
32. Miller, J. B. *et al.* Extraction of kinetic parameters in temperature programmed desorption: A comparison of methods. *J. Chem. Phys.* **87**, 6725 (1987).
33. Nieskens, D. L. S., van Bavel, A. P. & Niemantsverdriet, J. W. The analysis of temperature programmed desorption experiments of systems with lateral interactions; implications of the compensation effect. *Surf. Sci.* **546**, 159–169 (2003).
34. Avrami, M. Kinetics of Phase Change. I General Theory. *J. Chem. Phys.* **7**, 1103 (1939).
35. Avrami, M. Kinetics of Phase Change. II Transformation-Time Relations for Random Distribution of Nuclei. *J. Chem. Phys.* **8**, 212 (1940).
36. Avrami, M. Granulation, Phase Change, and Microstructure Kinetics of Phase Change. III. *J. Chem. Phys.* **9**, 177 (1941).
37. Fanfoni, M. & Tomellini, M. The Johnson-Mehl-Avrami-Kohnogorov model: A brief review. *Nuovo Cim. D* **20**, 1171–1182 (1998).
38. Farjas, J. & Roura, P. Modification of the Kolmogorov-Johnson-Mehl-Avrami rate equation for non-isothermal experiments and its analytical solution. *Acta Mater.* **54**, 5573–5579 (2006).
39. Berggaard, N. *et al.* Time-resolved photoelectron spectroscopy using synchrotron radiation time structure. *J. Synchrotron Radiat.* **18**, 245–250 (2011).
40. Himpfel, F., McFeely, F., Taleb-Ibrahimi, A., Yarmoff, J. & Hollinger, G. Microscopic structure of the SiO₂/Si interface. *Phys. Rev. B* **38**, 6084–6096 (1988).
41. Rochet, F. *et al.* Suboxides at the Si/SiO₂ interface: a Si2p core level study with synchrotron radiation. *J. Non. Cryst. Solids* **216**, 148–155 (1997).
42. Jolly, F., Rochet, F., Dufour, G., Grupp, C. & Taleb-Ibrahimi, A. Oxidized silicon surfaces studied by high resolution Si 2p core-level photoelectron spectroscopy using synchrotron radiation. *J. Non. Cryst. Solids* **280**, 150–155 (2001).
43. Le Lay, G. *et al.* Surface core-level shifts of Si(111)7 × 7: A fundamental reassessment. *Phys. Rev. B* **50**, 14277–14282 (1994).
44. Yamamoto, S. & Matsuda, I. Time-Resolved Photoelectron Spectroscopies Using Synchrotron Radiation: Past, Present, and Future. *J. Phys. Soc. Japan* **82**, 21003 (2013).
45. Lizzit, S. & Baraldi, A. High-resolution fast X-ray photoelectron spectroscopy study of ethylene interaction with Ir(111): From chemisorption to dissociation and graphene formation. *Catal. Today* **154**, 68–74 (2010).
46. Nambu, A. *et al.* An ultrahigh-speed one-dimensional detector for use in synchrotron radiation spectroscopy: first photoemission results. *Journal of Electron Spectroscopy and Related Phenomena* 137–140, 691–697 (2004).
47. Bennett, P. A. & Webb, M. W. The Si(111)7 × 7 to '1 × 1' transition. *Surf. Sci.* **104**, 74–104 (1981).
48. Teliaps, W. & Bauer, E. The (7 × 7) ↔ (1 × 1) phase transition on Si(111). *Surf. Sci.* **162**, 163–168 (1985).
49. Kruse, J. E. *et al.* Selective-area growth of GaN nanowires on SiO₂-masked Si (111) substrates by molecular beam epitaxy. *J. Appl. Phys.* **119**, 224305 (2016).
50. Zhao, W. *et al.* Analysis of the Si(111) surface prepared in chemical vapor ambient for subsequent III-V heteroepitaxy. *Appl. Surf. Sci.* **392**, 1043–1048 (2017).
51. Flege, J. I. *et al.* Ultrathin, epitaxial cerium dioxide on silicon. *Appl. Phys. Lett.* **104**, 131604 (2014).
52. Hollinger, G. & Himpfel, F. Multiple-bonding configurations for oxygen on silicon surfaces. *Phys. Rev. B* **28**, 3651–3653 (1983).
53. Jolly, F., Rochet, F., Dufour, G., Grupp, C. & Taleb-Ibrahimi, A. Oxidized silicon surfaces studied by high resolution Si 2p core-level photoelectron spectroscopy using synchrotron radiation. *J. Non. Cryst. Solids* **280** (2001).
54. Karlsson, C., Landemark, E., Chao, Y.-C. & Uhrberg, R. Atomic origins of the surface components in the Si 2p core-level spectra of the Si(111)7 × 7 surface. *Phys. Rev. B* **50**, 5767–5770 (1994).
55. Gelius, U. *et al.* A high resolution multipurpose ESCA instrument with X-ray monochromator. *Nucl. Instruments Methods Phys. Res. Sect. B Beam Interact. with Mater. Atoms* **1**, 85–117 (1984).
56. Hollinger, G. Oxygen chemisorption and oxide formation on Si(111) and Si(100) surfaces. *J. Vac. Sci. Technol. A Vacuum, Surfaces, Film.* **1**, 640 (1983).
57. Losio, R., Altmann, K. N. & Himpfel, F. J. Fermi surface of Si(111)7 × 7. *Phys. Rev. B* **61**, 10845–10853 (2000).
58. Ohdomari, I., Watanabe, T., Kumamoto, K. & Hoshino, T. Consideration of atom movement during Si surface reconstruction. *Phase Transitions* **62**, 245–258 (1997).
59. Paggel, J. J. *et al.* Correlation of surface core levels and structural building blocks for the Si(111)-7 × 7 reconstruction through high-resolution core-level spectroscopy. *Phys. Rev. B* **50**, 18686–18689 (1994).
60. Höfer, U., Li, L., Ratzlaff, G. A. & Heinz, T. F. Nonlinear optical study of the Si(111)7 × 7 to 1 × 1 phase transition: Superheating and the nature of the 1 × 1 phase. *Phys. Rev. B* **52**, 5264–5268 (1995).
61. Štich, I., Payne, M. C., King-Smith, R. D., Lin, J.-S. & Clarke, L. J. Ab initio total-energy calculations for extremely large systems: Application to the Takayanagi reconstruction of Si(111). *Phys. Rev. Lett.* **68**, 1351–1354 (1992).
62. Becker, R. S., Golovchenko, J. A., Higashi, G. S. & Swartzentruber, B. S. New Reconstructions on Silicon (111) Surfaces. *Phys. Rev. Lett.* **57**, 1020–1023 (1986).
63. Zhachuk, R., Teys, S. & Coutinho, J. Strain-induced structure transformations on Si(111) and Ge(111) surfaces: A combined density-functional and scanning tunneling microscopy study. *J. Chem. Phys.* **138**, 224702 (2013).

64. Frank, S. & Rikvold, P. A. Kinetic Monte Carlo simulations of electrodeposition: Crossover from continuous to instantaneous homogeneous nucleation within Avrami's law. *Surf. Sci.* **600**, 2470–2487 (2006).
65. Polack, F. *et al.* Progress report and first results of new Super-ACO beamlines. in *Proceedings of SPIE - The International Society for Optical Engineering* **3450**, (1998).
66. Kinahan, N. T. *et al.* Site-Specific Evolution of Surface Stress during the Room-Temperature Oxidation of the Si(111)–(7 × 7) Surface. *Phys. Rev. Lett.* **104**, 146101 (2010).
67. Sakamoto, K., Zhang, H. M. & Uhrberg, R. I. G. Observation of two metastable oxygen species adsorbed on a Si(7 × 7) surface: Reinterpretation of the initial oxidation process. *Phys. Rev. B* **68**, 75302 (2003).
68. Sakamoto, K., Zhang, H. M. & Uhrberg, R. I. G. Photoemission study of metastable oxygen adsorbed on a Si(111)–7 × 7 surface. *Phys. Rev. B* **70**, 35301 (2004).
69. Moore, J. C., Skrobiszewski, J. L. & Baski, A. A. Sublimation behavior of SiO₂ from low- and high-index silicon surfaces. *J. Vac. Sci. Technol. A Vacuum, Surfaces, Film.* **25**, 812 (2007).
70. Kissinger, H. E. Reaction Kinetics in Differential Thermal Analysis (2002).

Author Contributions

All authors discussed the organization and content of the manuscript. J.J.G. participated to the experiments, designed the procedures enabling the data analysis and the fitting procedures of the core-level spectra. M.G.S. implemented the synchronized annealing stage and participated to the experiments. M.E.K. implemented the synchronized temperature monitoring stage and participated to the experiments. F.B. participated to the experiment and edited the manuscript. F.R. and F.S. co-wrote the paper. F.S. designed the fast photoemission measurement setup and participated to the experiment. F.R. proposed the de-oxidation experiment, participated to the experiment, and performed the mathematical calculations of the Avrami analysis.

Additional Information

Supplementary information accompanies this paper at <https://doi.org/10.1038/s41598-017-14532-4>.

Competing Interests: The authors declare that they have no competing interests.

Publisher's note: Springer Nature remains neutral with regard to jurisdictional claims in published maps and institutional affiliations.



Open Access This article is licensed under a Creative Commons Attribution 4.0 International License, which permits use, sharing, adaptation, distribution and reproduction in any medium or format, as long as you give appropriate credit to the original author(s) and the source, provide a link to the Creative Commons license, and indicate if changes were made. The images or other third party material in this article are included in the article's Creative Commons license, unless indicated otherwise in a credit line to the material. If material is not included in the article's Creative Commons license and your intended use is not permitted by statutory regulation or exceeds the permitted use, you will need to obtain permission directly from the copyright holder. To view a copy of this license, visit <http://creativecommons.org/licenses/by/4.0/>.

© The Author(s) 2017